

Microwave spectroscopic study of the hyperfine structure of antiprotonic ^3He

S Friedreich¹, D Barna^{2,3}, F Caspers⁴, A Dax², R S Hayano²,
M Hori^{2,5}, D Horváth^{3,6}, B Juhász^{1‡}, T Kobayashi²,
O Massiczek¹, A Sótér⁵, K Todoroki², E Widmann¹ and
J Zmeskal¹

¹Stefan Meyer Institute for Subatomic Physics, Austrian Academy of Sciences, Boltzmannngasse 3, A-1090 Vienna, Austria

²Department of Physics, University of Tokyo, 7-3-1 Hongo, Bunkyo-ku, Tokyo 113-0033, Japan

³Wigner Research Centre for Physics, Institute for Particle and Nuclear Physics, H-1121 Budapest, Konkoly-Thege 29-33, Hungary

⁴CERN, CH-1211 Geneva, Switzerland

⁵Max-Planck-Institut für Quantenoptik, Hans-Kopfermann-Strasse 1, D-85748 Garching, Germany

⁶Institute of Nuclear Research of the Hungarian Academy of Sciences, H-4001 Debrecen, PO Box 51, Hungary

E-mail: susanne.friedreich@oeaw.ac.at

Abstract. In this work we describe the latest results for the measurements of the hyperfine structure of antiprotonic ^3He . Two out of four measurable super-super-hyperfine SSHF transition lines of the $(n, L) = (36, 34)$ state of antiprotonic ^3He were observed. The measured frequencies of the individual transitions are 11.12548(08) GHz and 11.15793(13) GHz, with an increased precision of about 43% and 25% respectively compared to our first measurements with antiprotonic ^3He [S. Friedreich *et al.*, Phys. Lett. B 700 (2011) 1–6]. They are less than 0.5 MHz higher with respect to the most recent theoretical values, still within their estimated errors. Although the experimental uncertainty for the difference of 0.03245(15) GHz between these frequencies is large as compared to that of theory, its measured value also agrees with theoretical calculations. The rates for collisions between antiprotonic helium and helium atoms have been assessed through comparison with simulations, resulting in an elastic collision rate of $\gamma_e = 3.41 \pm 0.62$ MHz and an inelastic collision rate of $\gamma_i = 0.51 \pm 0.07$ MHz.

Version 24 November 2021

PACS numbers: 36.10.-k, 32.10.Fn, 33.40.+f

Submitted to: *Journal of Physics B*

‡ Present address: Lufthansa Systems Hungária Kft., Neumann János utca 1/E, H-1117 Budapest

1. Introduction

1 Antiprotonic helium $\bar{\text{p}}\text{He}^+$ is a metastable three-body system consisting of one electron
 2 in the ground state, the helium nucleus and one antiproton [1–4]. This *exotic* atom can
 3 be created whenever an antiproton in the vicinity of a helium atom is slowed down to
 4 its ionization energy of ~ 24.6 eV or below. The antiproton can eject one of the two
 5 electrons from the ground state and replace it. The antiproton is captured and, due to its
 6 high mass, most likely to be in states with high angular momentum and with principal
 7 quantum number $n = n_0 \equiv \sqrt{M^*/m_e} \sim 38$, M^* being the reduced mass of the system,
 8 while the electron remains in the ground state. Therefore, these newly-formed atoms
 9 occupy circular states with L close to n , where L is the angular momentum quantum
 10 number.

11 A majority of 97% of these exotic atoms find themselves in states dominated by
 12 Auger decay. Due to the Auger excitation of the electron they ionize within a few
 13 nanoseconds after formation. The remaining 3% of antiprotonic helium atoms remain
 14 in metastable, radiative decay-dominated states. These states are relatively long lived,
 15 having a lifetime of about 1-2 μs – a time window that can be used to do laser and
 16 microwave spectroscopy measurements [5–7].

2. Hyperfine structure of antiprotonic helium

17 The interaction of magnetic moments between electron, antiproton and helium nucleus
 18 gives rise to a splitting of the $\bar{\text{p}}{}^3\text{He}^+$ energy levels. The coupling of the electron spin \vec{S}_e
 19 and the orbital angular momentum of the antiproton \vec{L} leads to the primary splitting of
 20 the state into a doublet structure, referred to as *hyperfine (HF) splitting*. The angular
 21 momentum $\vec{F} = \vec{L} + \vec{S}_e$ defines the two substates with quantum numbers $F_+ = L + \frac{1}{2}$
 22 and $F_- = L - \frac{1}{2}$. The non-zero spin of the ${}^3\text{He}$ nucleus causes a further, so-called
 23 *super-hyperfine (SHF) splitting*, which can be characterized by the angular momentum
 24 $\vec{G} = \vec{F} + \vec{S}_h = \vec{L} + \vec{S}_e + \vec{S}_h$, where \vec{S}_h is the spin of the helium nucleus. This results in
 25 four SHF substates. At last, the spin-orbit interaction of the antiproton orbital angular
 26 momentum and antiproton spin \vec{S}_p in combination with the contact spin-spin and the
 27 tensor spin-spin interactions between the particles result in a further splitting of the SHF
 28 substates into eight substates which we call *super-super-hyperfine (SSH) splitting*. This
 29 octuplet structure can be described by the angular momentum $\vec{J} = \vec{G} + \vec{S}_p = \vec{L} + \vec{S}_e + \vec{S}_h +$
 30 \vec{S}_p . Even though the magnetic moment of the antiproton is larger than that of the ${}^3\text{He}$
 31 nucleus, the former has a smaller overlap with the electron cloud. Therefore it creates
 32 a smaller splitting. The complete hyperfine structure for $\bar{\text{p}}{}^3\text{He}^+$ is illustrated in Fig. 1.

33

34 The interest in $\bar{\text{p}}{}^3\text{He}^+$ arises from an additional contribution to the hyperfine
 35 structure caused by the coupling of the nuclear spin to the antiproton orbital momentum
 36 with respect to $\bar{\text{p}}{}^4\text{He}^+$ [5]. Such a measurement would allow a more rigorous test
 37 of QED theory. The accurate knowledge of the hyperfine structure of antiprotonic

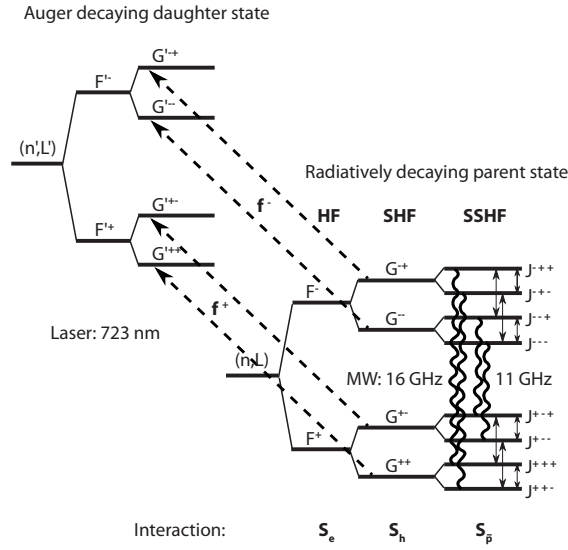


Figure 1: A schematic drawing of the laser-microwave-laser method. The dashed arrows indicate the laser transitions between the SHF levels of the radiative decay-dominated state $(n, L) = (36, 34)$ and the Auger decay-dominated state $(37, 33)$ of $\bar{\text{p}}^3\text{He}^+$. The wavy lines illustrate the microwave-induced transitions between the SSHF levels of the long-lived state.

38 helium is essential for the calculation of the laser transition energies at the level of ppb
 39 accuracy needed for comparison to laser spectroscopy experiments and the extraction
 40 of the antiproton-to-electron mass ratio [7]. An experimental verification of the HFS
 41 splitting in $\bar{\text{p}}^3\text{He}^+$ is therefore of great importance.

42 The calculations of the hyperfine structure were developed by two different
 43 groups [8–12]. This series of experiments, studying the $(n, L) = (36, 34)$ state, was
 44 the first attempt to measure the microwave transition frequencies between hyperfine
 45 substates of $\bar{\text{p}}^3\text{He}^+$. Transitions between the SSHF states were induced by a magnetic
 46 field oscillating in the microwave frequency range. Due to technical limitations of the
 47 microwave input power, only the transitions which flip the spin of the electron could
 48 be measured. There are four such "allowed" SSHF transitions for the $(n, L) = (36, 34)$
 49 state of $\bar{\text{p}}^3\text{He}^+$ two of which we investigated with the present work:

$$\begin{aligned} \nu_{\text{HF}}^{--} &: J^{---} = L - \frac{3}{2} \longrightarrow J^{+--} = L - \frac{1}{2} \\ \nu_{\text{HF}}^{-+} &: J^{--+} = L - \frac{1}{2} \longrightarrow J^{+++} = L + \frac{1}{2} \end{aligned}$$

50 3. Laser-microwave-laser spectroscopy

51 The first observation of a hyperfine structure in antiprotonic helium was achieved in
 52 a laser scan of the $(n, L) = (37, 34) \rightarrow (38, 35)$ transitions in $\bar{\text{p}}^4\text{He}^+$ [13]. Due to the
 53 limited precision achievable in a laser scan, a *laser-microwave-laser method* (Fig. 1) was
 54 introduced in [14]. It is based on a three-step process involving laser and microwave
 55 stimulated resonance transitions.

56 After antiprotonic helium is formed, the atoms in the hyperfine substates are
 57 all equally populated. Therefore at first a population asymmetry between the SSHF
 58 substates of the measured radiative decay state (n, L) needs to be created. This
 59 depopulation is induced by a short laser pulse which transfers the majority of an-
 60 tiprotons from one of the HF states of the radiative decay-dominated, metastable
 61 parent state to an Auger decay-dominated, short-lived daughter state. In this ex-
 62 periment the f^+ transition is used. The bandwidth of the laser (100 MHz) and
 63 Doppler broadening at 6 K (300 MHz) are small enough compared to the difference
 64 of $f^- - f^+ \sim 1.7$ GHz so that the f^- transition is not affected and a population
 65 asymmetry can be achieved. The antiprotons in the short-lived state annihilate within
 66 a few nanoseconds. In the next step, a microwave frequency pulse tuned around the
 67 transition frequency between two SSHF substates of the metastable state is applied. If
 68 the microwave field is on resonance with one of these transitions, it will cause a pop-
 69 ulation transfer and thus partial refilling of one of the previously depopulated states.
 70 A second laser pulse will then again cause depopulation of the same HF substate and
 71 subsequently Auger decay of the transferred atoms and annihilation of the antipro-
 72 tons in the nucleus will occur. The number of annihilations after the second laser
 73 pulse will be the larger the more antiprotons were transferred by the microwave pulse.

74
 75 When the antiprotons first enter the helium gas, a large annihilation peak ("prompt
 76 peak") is caused by the majority of formed $\bar{\text{p}}\text{He}^+$ atoms which find themselves in Auger
 77 decay-dominated states and annihilate within picoseconds after formation. At later
 78 times, this peak exhibits an exponential tail due to $\bar{\text{p}}\text{He}^+$ atoms in the metastable
 79 states cascading more slowly towards the nucleus. This constitutes the background
 80 for the laser-induced annihilation signals. The daughter state has a very short life-
 81 time of ~ 10 ns and thus the population transfer is indicated by a sharp annihila-
 82 tion peak against the background during the two laser pulses. The area under these
 83 peaks is proportional to the population transferred to this short-lived state. This spec-
 84 trum, with the two laser-induced peaks super-imposed on the exponential tail – as
 85 displayed in Fig. 2 – is called *analogue delayed annihilation time spectrum* or ADATS.

86
 87 Since the intensity of the antiproton pulse fluctuates from shot to shot, the peaks
 88 must be normalised by the total intensity of the pulse (total). This ratio is referred to
 89 as *peak-to-total*. The peak-to-total (ptt) corresponds to the ratio of the peak area ($I(t_1)$
 90 or $I(t_2)$) to the total area under the full spectrum. If the second laser annihilation
 91 peak is further normalised to the first one, the total cancels out. The frequencies of
 92 the two SSHF transitions can now be obtained as distinct lines by plotting $I(t_2)/I(t_1)$
 93 as a function of the microwave frequency. The ratio $I(t_2)/I(t_1)$ is largely independent
 94 of intensity and position fluctuations of the antiproton beam. The intensity of the
 95 transition lines is subject to the time delay between the two laser pulses and thus also
 96 to collisional relaxation processes [15–18]. This means that, once the first laser has
 97 caused depopulation, the system will start to relax through spin exchanging collisions

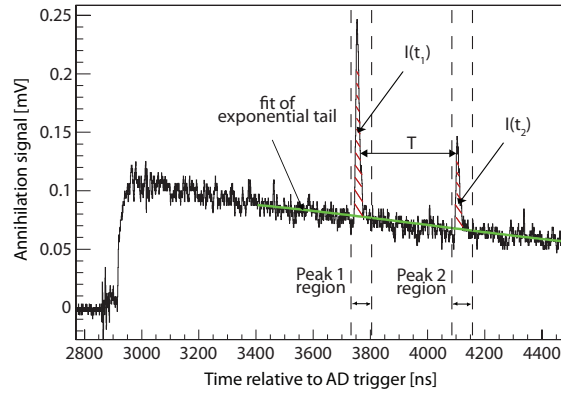


Figure 2: A part of the analog delayed annihilation time spectrum (ADATS) with the two laser-stimulated annihilation peaks against the exponential decaying background of the metastable cascade. T denotes the delay time between the two laser pulses. The photomultipliers of the Cherenkov counters used to record this spectrum are gated off during the initial \bar{p} pulse arrival [19]. Thus, the prompt peak is cut off below 2900 ns and only the annihilations due to the metastable state depopulation are recorded.

98 between antiprotonic helium atoms and regular helium atoms. Refilling from higher-
 99 lying states also contributes to the equalization of the hyperfine substate populations.
 100 In general, a short delay T is preferable because the signal height will decrease for
 101 longer laser delay times as a result of the exponential decay of the metastable state
 102 populations. However, the linewidth of the RF transition will increase if the delay is too
 103 short. Further, far higher RF power will be required to complete one spin-flip. If the
 104 delay is too long, the collisional relaxation of the system would already have eliminated
 105 any asymmetry between the two states caused by the first laser pulse. The signal would
 106 be too low to be observed.

107 The two pulsed lasers were fixed to a wavelength of 723.877 nm, with a pulse
 108 length of 8-12 ns, to induce the f^+ laser transition between the $(n, L) = (36, 34)$ and
 109 the $(n', L') = (37, 33)$ state. The pulse length should be comparable to or longer
 110 than the Auger lifetime of the short-lived state. Generally spoken, the longer the
 111 laser pulse the larger the achieved depopulation and thus the resulting annihilation
 112 signal. The depopulation also depends on the laser pulse energy. It is important to
 113 find the appropriate laser fluence where the power is saturated and therefore the laser
 114 depletion efficiency is optimized in order to avoid power broadened resonance lines and
 115 as a consequence partial depopulation of the other HF transition line f^- . For this
 116 experiment a pulse-amplified continuous-wave laser system with a narrow linewidth of
 117 about 100 MHz was used [20]. The laser fluence was in the range of 20-40 mJ/cm², the
 118 laser waist ~ 5 mm, leading to a depletion efficiency of about 90% – based on numerical
 119 simulations of the laser transition processes [18].

120 There are several limitations to the choice of the measured state, such as availability
 121 of a laser source in the required frequency range or the splitting of the transitions
 122 between the HF states of the daughter and the parent state. The laser transition

123 between the $(n, L) = (36, 34)$ and the $(n', L') = (37, 33)$ state was chosen because it
 124 is easily stimulated and the primary population is large, thus leading to a large signal.
 125 The captured fraction of antiprotons in the measured metastable state $(n, L) = (36, 34)$
 126 is $(3-4) \times 10^{-3}$ [21].

127 **4. Experimental setup**

128 The antiprotons for the experiment are provided by the AD (Antiproton Decelerator)
 129 at CERN [22], with a pulsed beam of $(1-3) \times 10^7$ antiprotons at an energy of 5.3 MeV,
 130 a pulse length of 100-300 ns, and a repetition interval of about 100 s. The particles
 131 are stopped in a helium gas target, with a gas pressure of 250 mbar, cooled down to a
 132 temperature of about 6 K. This target is built as a cylindrical chamber whose axis is
 133 parallel to the beam direction and which is designed to act also as a microwave cavity
 134 resonating in the TM_{110} mode. The faces of the cylindrical cavity have a 25 μm thick

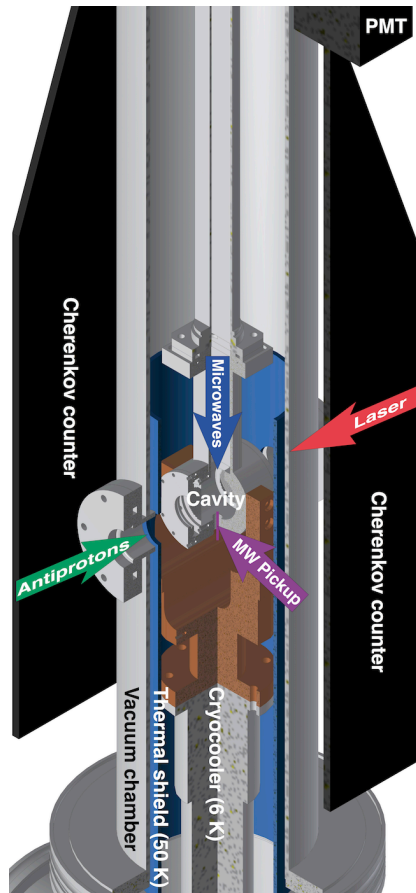


Figure 3: Central part of the experimental setup. Antiproton and laser beams coming from opposite sides are injected into the microwave cavity which also contains the helium gas. Microwaves are fed through a wave guide from top, and the microwave power is measured by a small antenna. Outside the vacuum chamber two Cherenkov counters are mounted to detect the pions resulting from the annihilations.

135 titanium window for the antiproton beam and a 4 mm thick fused silica window for the
136 laser beam to enter [23], and are equipped with meshes to contain the microwaves.

137 In order to measure the annihilation decay products two Cherenkov counters are
138 mounted around the target volume, connected to photomultipliers (cf. Fig. 3) . They
139 are gated off during the initial \bar{p} pulse arrival [19] in order to count only the photons
140 arriving from the induced annihilations. A vector network analyzer (VNA, Rhode &
141 Schwarz ZVB20) synthesizes the microwave pulse that is further amplified by a travelling
142 wave tube amplifier (TWTA, TMD PTC6358) from where a waveguide system transmits
143 the pulse of $\sim 20 \mu\text{s}$ length to the cavity. The waveguide is over-coupled to the cavity
144 resulting in a low quality factor of $Q = 160$. The frequency of the microwave radiation is
145 tuned by changing the frequency of the VNA, increasing the input power off-resonance
146 so to keep the power inside the cavity constant. The microwave power inside the
147 cavity is measured by a pickup antenna and a calibrated diode (Agilent 8474B). Input
148 powers of maximum 40 W were used to achieve a constant power of 7.5 W inside the
149 cavity. A detailed discussion on the microwave apparatus, including design, simulation,
150 construction and calibration, can be found in [24].

151 A cryostat with compressor-based cooling system was built to cool the experimental
152 apparatus without abundant use of coolants, to allow an efficient cooling procedure and
153 thus little loss of measurement time. The microwave cavity is filled with helium gas
154 and cooled down directly to about 6 K by mounting it on a coldhead [23]. By use of
155 additional degrader foils (Polyimide film foils § of about $70 \mu\text{m}$ thickness) the antiprotons
156 could be stopped in the center of a cavity in a volume of about 1 cm^2 [25].

157 5. Results

158 In preparation for the actual investigation of the hyperfine substructure, via microwave
159 resonance, several studies are required to optimize the parameters such as laser power,
160 laser resonance frequency, laser delay time and microwave power.

161 The frequency and the splitting of the two resonance lines f^+ and f^- are determined
162 by scanning our laser system over a range of about 5 GHz centered around the two
163 transition frequencies. The laser power was adjusted to observe a clear splitting of
164 the two transition lines to ensure that only one of the two hyperfine levels of the
165 $(n, L) = (36, 34)$ state is depopulated by laser stimulation. The measurements were
166 all performed at a target pressure of 250 mbar and a delay time of $T = 350 \text{ ns}$ between
167 the two lasers pulses. Due to limited measurement time, only one target density was
168 used. However, previous studies in $\bar{p}^4\text{He}^+$ [5] as well as calculations suggest that the
169 target density should have no effect on the resonance line shape, width or amplitude of
170 the resonance lines [15–18] at the level of the precision of this experiment.

171 It is important to choose the correct microwave power in order for the electron to
172 undergo one electron spin-flip [24], i.e. to achieve a π -pulse that results in the highest
173 signal. For this the ptt ratio is measured at the predicted resonance frequency for several

§ Upilex foil made by UBE Industries

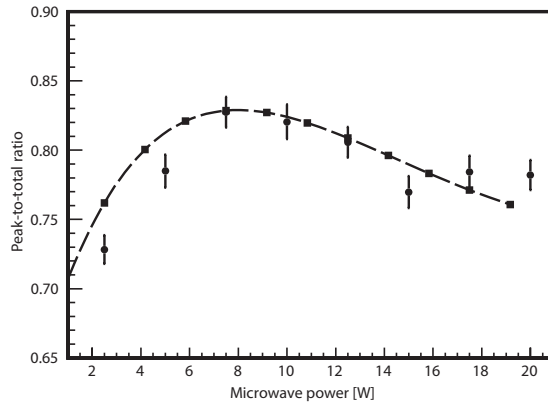


Figure 4: Signal-to-noise ratio measured for several microwave powers in comparison to a numerical simulation based on the used measurement parameters and normalised to the measured signal amplitude [18]. The given power value is referring to the the power inside the target. 7.5 W were finally chosen for the microwave spectroscopic measurements.

174 power values in the range between 0 and 20 Watts microwave power inside the cavity,
 175 as determined by the pick-up antenna. The points measured at 0 W were recorded on
 176 resonance. Points were also taken sufficiently off resonance (a few hundred Megahertz
 177 away) but at some non-zero power. Off resonance, the microwave pulse should have no
 178 effect on the atoms, thus confirming that the observed signal is real and not caused by
 179 some kind of fluctuations. Fig. 4 illustrates such a scan. According to these data, a
 180 π -pulse is completed at the first power maximum of about 7.5 W. The microwave power
 181 study is performed for a laser delay of 350 ns.

182 Figure 5 displays the frequency dependence of the microwave power over the scan
 183 range in the case of the two 11 GHz transitions – with an average drift of 10-13% over
 184 the recorded spectrum. Despite thorough calibration of the system, there appears to be
 185 a linear tendency of the power over the frequency range. This behavior could potentially
 186 lead to a distortion of the line shape and an increase of errors. However, from Fig. 4
 187 can be seen that the peak-to-total ratio does not change considerably within the error
 188 between a microwave power of 7.5 W and 10 W. Therefore, it is not expected that this
 189 linear tendency of the power over the frequency range has a significant effect on the
 190 error and the fit of the transitions lines.

191 5.1. The microwave transitions

192 Two of the four allowed SSHF resonance transitions in $\bar{p}{}^3\text{He}^+$ could be observed. In
 193 the analysis all recorded data, including the previously published data of 2010 [6]
 194 and new ones obtained in 2011 were taken into account. The two resonances were
 195 measured and fitted separately. For each microwave frequency scan 20-25 frequency
 196 points were recorded, equally spaced over a range of 9 MHz, centered around the
 197 theoretical transition frequency. Two analysis methods were used to average over data
 198 taken in different years and under different conditions: *average scan fitting (ASF)* in the

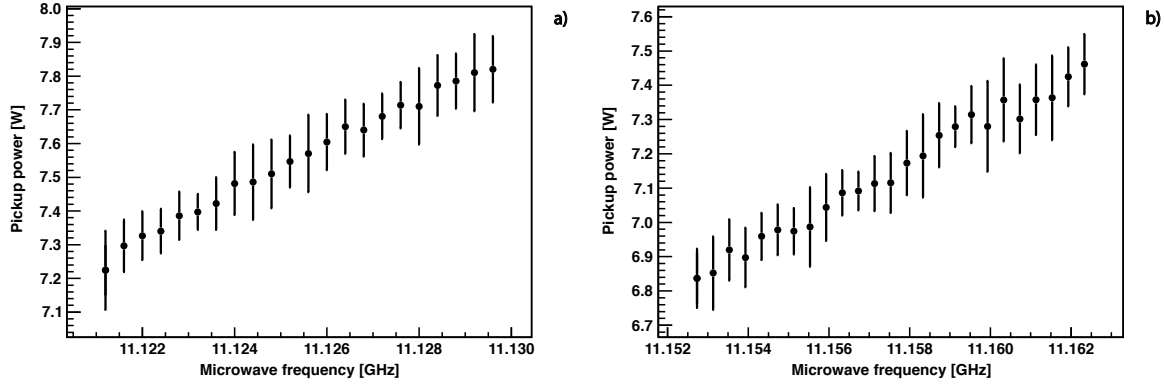


Figure 5: The change of the microwave power over the measured frequency range for the a) 11.125 GHz and the b) 11.157 GHz transition.

199 case of identical conditions and frequency points, the data taken at the same frequency
 200 were first averaged using the method of weighted average, then the resulting scan was
 201 fitted. For *simultaneous individual scan fitting (ISF)* the data points were not averaged
 202 but simultaneously fitted using the same values for central frequency and width but
 203 individual values for height or background levels. Using ISF, also scans taken with
 204 different microwave power or with different frequency points can be analyzed together.
 205 In the case of the 11.125 GHz transition the value for every frequency was averaged
 206 over a total of 40 data points, for the 11.157 GHz over a total of 42 data points. These
 207 values were obtained using the simultaneous fitting of individual scans. The fit results
 are displayed in Fig. 6 in comparison with simulation curves.

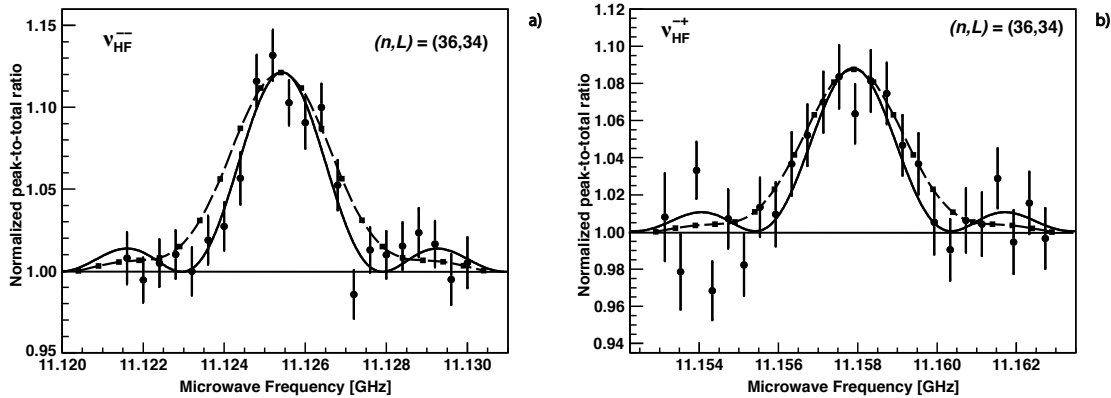


Figure 6: Scan over the microwave frequency for the a) ν_{HF}^- and the b) ν_{HF}^+ transition of the $(n, L) = (36, 34)$ state in $\bar{\text{p}}^3\text{He}^+$, at a target pressure of 250 mbar, fitted with Eq. 1 (solid line) and using the simultaneous fitting of individual scans. The frequency of the measured transitions are $\nu_{\text{HF}}^- = 11.12548(08)$ GHz and $\nu_{\text{HF}}^+ = 11.15793(13)$ GHz. The dashed curve shows a simulation using collision rates obtained from comparison between experiment and simulation [18].

209

210 To fit the two transitions, a function of the natural line shape for a two-level system
 211 which is affected by an oscillating magnetic field for a time T was used. It is given by [26]

$$\begin{aligned}
 X(\omega) &= A \frac{|2b|^2}{|2b|^2 + (\omega_0 - \omega)^2} \\
 &\times \sin^2 \left\{ \frac{1}{2} \left[|2b|^2 + (\omega_0 - \omega)^2 \right]^{\frac{1}{2}} T \right\}.
 \end{aligned}
 \tag{1}$$

212 Here $X(\omega)$ is the probability that an atom is transferred from one HF state to the other,
 213 ω is the angular frequency of the magnetic field and ω_0 is the angular frequency of the
 214 transition between the two energy levels. A is a scaling term which equals 1 in an ideal
 215 two-level system. In the fitting procedure this term takes into account that in reality
 216 the two-level system is not ideal. The parameter $b = \Omega/2$ is a time independent part
 217 of the transition matrix elements between two energy levels, with the Rabi frequency
 218 $\Omega(\mu B_0)/\hbar$ and μ denoting the calculated averaged magnetic dipole moment. The Rabi
 219 frequency is dependent on the microwave power. Using the calculated values for the
 220 average oscillating magnetic field amplitude of $B_0 = 0.24(4) \times 10^{-4}$ T and the magnetic
 221 dipole moment, we obtain a Rabi frequency in the range of 10 MHz. In the case of a
 222 complete π -pulse, one obtains $|b|T = \pi/2$. This is referred to as the optimum case, since
 223 together with $X(\omega) = 1$ at resonance this gives the smallest width for the transition
 224 line, $\Gamma = 0.799/T = 2.28$ MHz for $T = 350$ ns. The two observed microwave resonance
 225 transitions were measured and fitted individually with this function, adding a constant
 226 background. The side peaks in the fit are caused by the Rabi oscillations. From the fit,
 227 the frequencies for the measured ν_{HF}^{--} and ν_{HF}^{-+} transitions can be obtained.

228 As seen in Tab. 1 the fit results of the scans show a normalized χ^2/ndf that is
 229 larger than one. This is a general feature of our analog method to measure the delayed
 230 annihilation time spectra: the ADATS consists of the digitized current output of the

Table 1: The table displays the uncorrected fit results $\nu_{\text{HF}}^{\text{u}}$ for the fitting of the raw data together with the reduced χ^2/ndf and ν_{HF} after inflating the errors of the individual data points by $\sqrt{\chi^2/ndf}$. The fit transition frequencies are displayed for the two different fitting methods, ASF and ISF. At the higher resonance the frequency points differed slightly between 2010 and 2011. These data can only be combined in the averaging over all single scans. The microwave power for the 11.157 GHz resonance was further lower by about 2.5 W compared to 2011. Therefore, the values obtained by the ISF method were used as final results.

Transition	Method	$\nu_{\text{HF}}^{\text{u}}$ (GHz)	χ^2/ndf	ν_{HF} (GHz)
ν_{HF}^{--}	ASF	11.12550(04)	8.71	11.12550(08)
ν_{HF}^{--}	ISF	11.12548(03)	7.13	11.12548(08)
ν_{HF}^{-+} (2010)	ASF	11.15830(07)	8.26	11.15830(17)
ν_{HF}^{-+} (2011)	ASF	11.15760(07)	8.42	11.15760(14)
ν_{HF}^{-+}	ISF	11.15793(04)	7.92	11.15793(13)

Cherenkov PMTs that does not directly carry the statistical information on the observed number of annihilations per time. From the observed fluctuations, the digitization error, and other parameters a error is calculated that systematically underestimates the fluctuations in the data. Therefore the errors of all data points of a scan are multiplied by $\sqrt{\chi^2/ndf}$ to obtain the correct errors of the fit results.

Regarding the errors, there are several systematic effects which had to be considered. The largest influence was due to shot-to-shot fluctuations of the antiproton beam. These effects were reduced by normalizing to the total intensity of the pulse and further normalizing the second annihilation peak to the first one. Therefore, mainly shot-to-shot fluctuations of the microwave power and deviations in the laser position and fluence from day to day – although considerably smaller – contributed to the error quoted in Table 2. The individual contributions from fluctuations of antiproton beam and laser beam cannot be assessed separately. They are contained in the error obtained from the fit.

The laser power as well as the wavelength and the overlap between the two laser pulses were monitored and measured, concluding that the fluctuations give no relevant contribution to the measurement error. The mean laser energy changes by about 0.07% over one measurement shift of eight hours, the laser wavelength drifts by about 0.002%. It is difficult to quantify by how much fluctuations of the laser parameters influence the measured annihilation signal.

251

The transition processes were numerically simulated by solving the optical Bloch equations in order to estimate important measurement parameters, in particular the required microwave power and the signal-to-noise ratio [18]. The Bloch equations describe the depopulation of states, in this experiment induced by laser light and

Table 2: The experimental results for the ν_{HF}^{--} and ν_{HF}^{-+} in comparison with three-body QED calculations, where ν_{HF} denote the SSHF transition frequencies, δ_{exp} is the relative error of the measured frequencies and Γ the resonance line width. The relative deviation of experiment and theory is defined as $\delta_{\text{th-exp}} = (\nu_{\text{exp}} - \nu_{\text{th}})/\nu_{\text{exp}}$. The quoted theoretical precision is $\sim 5 \times 10^{-5}$ from the limitation of the Breit-Pauli approximation that neglects terms of relative order α^2 . This does not include numerical errors from the different variational methods used. For ref. [11] $\Delta\nu_{\text{HF}}^{\pm}$ was calculated from the difference of the tabulated antiproton spin-flip transitions $J^{--+} \rightarrow J^{---}$ and $J^{++} \rightarrow J^{+-}$, resulting in an relative error of 3×10^{-4} .

	ν_{exp} (GHz)	δ_{exp} $\times 10^6$	Γ (MHz)	Korobov [12,27] (GHz)	$\delta_{\text{th-exp}}$ $\times 10^6$	Kino [11] (GHz)	$\delta_{\text{th-exp}}$ $\times 10^6$
ν_{HF}^{--}	11.125 48(08)	7.2	1.69(11)	11.125 00(56)	43	11.125 15(56)	29
ν_{HF}^{-+}	11.157 93(13)	11.7	2.20(15)	11.157 73(56)	18	11.157 56(56)	33
		$\times 10^3$			$\times 10^3$		$\times 10^3$
$\Delta\nu_{\text{HF}}^{\pm}$	0.032 45(15)	4.7		0.032 721 9(16)	-8.4	0.032 408(11)	1.3

256 microwave radiation and under the influence of collisional effects. For most parameters,
 257 such as microwave power, Q value and laser delay, the measured values were taken.
 258 To assess the rates of collisional effects which induce relaxations between the SSHF
 259 states, the simulations are adjusted to the experimental results. Two types of collisions
 260 can be distinguished - elastic and inelastic collisions. While elastic collisions can cause
 261 a broadening and shift of the resonance line, inelastic collisions will result in a spin
 262 exchange between the hyperfine substates which can lead to a decrease of the measured
 263 signal. Both, elastic collision rate γ_e and inelastic collision rate γ_i , can have considerable
 264 systematic effects on the signal height, line shape and frequency of the transition line.
 265 The resulting calculated resonance curves are represented as dashed lines in Fig. 6,
 266 showing good agreement with the experimental data. Extracting the elastic and inelastic
 267 collision rates γ_e and γ_i for the two transitions gives

$$\begin{aligned}
 \text{for } 11.125 \text{ GHz : } \gamma_e^{--} &= 3.45^{+0.79}_{-0.71} \text{ MHz} & \text{for } 11.157 \text{ GHz : } \gamma_e^{-+} &= 3.48^{+1.20}_{-0.99} \text{ MHz} \\
 \gamma_i^{--} &= 0.51^{+0.09}_{-0.08} \text{ MHz} & \gamma_i^{-+} &= 0.52^{+0.13}_{-0.11} \text{ MHz} \quad (2)
 \end{aligned}$$

268 To obtain the errors for these rates, the annihilation signal amplitude was calculated for
 269 different values of the elastic and the inelastic collision rates for both transitions. The
 270 fitted annihilation signal amplitude of the transitions and its errors were then used to
 271 assess the collision rates for the minimum and maximum amplitude values within the
 272 $\pm 1\sigma$ level by interpolation.

273 Based on theory, the collision rates are expected to be equal for different single
 274 electron spin flip transitions within a state [17]. To calculate the weighted mean
 275 of the values for the individual transitions, a mathematical model presented in [28]
 276 which accounts for the asymmetric errors of the single values is used, resulting in
 277 an elastic collision rate of $\gamma_e = 3.41 \pm 0.62$ MHz and an inelastic collision rate of
 278 $\gamma_i = 0.51 \pm 0.07$ MHz. These rates go into the optical Bloch equations in the simulations
 279 as angular frequencies. Thus, in order to compare them to the total line widths
 280 $\Gamma = 0.799/T$ of the measured resonances (see Table 2), given as linear frequencies,
 281 they have to be divided by 2π :

$$\begin{aligned}
 \gamma'_e &= \frac{\gamma_e}{2\pi} = 0.54 \pm 0.10 \text{ MHz} \\
 \gamma'_i &= \frac{\gamma_i}{2\pi} = 0.08 \pm 0.01 \text{ MHz.} \quad (3)
 \end{aligned}$$

282 Only the elastic collision rate affects the width of the resonance line while inelastic
 283 collisions affect the transition rate and thus the height of the resonance signal. The
 284 measured rates agree within a factor 2 with theoretical calculations which obtain
 285 an elastic collision rate of approximately 0.48 MHz and an inelastic collision rate of
 286 approximately 0.16 MHz, given as linear frequencies [17].

287 6. Conclusion

288 Two of the four favored SSHF resonance transitions in $\bar{\text{p}}^3\text{He}^+$ were observed and are in
 289 agreement with theory within the estimated theoretical error (cf. Tab. 2 and Fig. 7). The

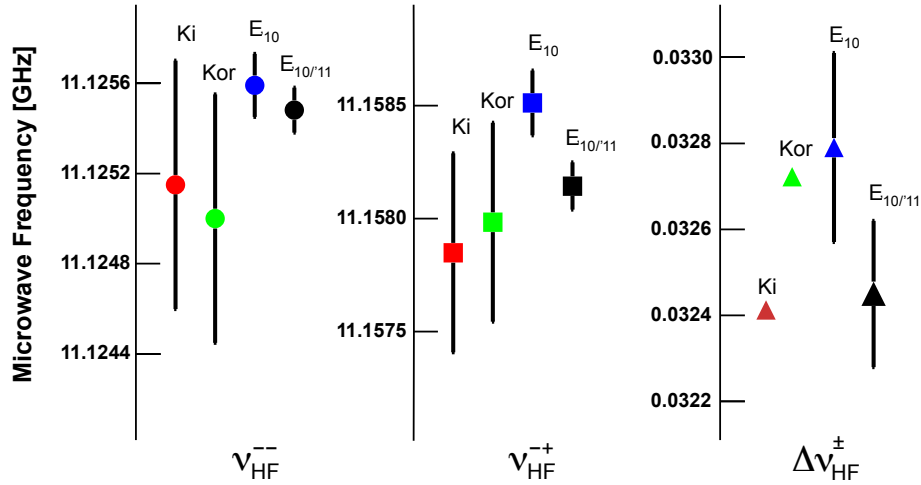


Figure 7: This graph summarizes the results for the two measured *SSH*F transitions ν_{HF}^{--} and ν_{HF}^{+} as well as the frequency difference $\Delta\nu_{\text{HF}}^{\pm}(E_{10} [6], E_{10/11})$ for the first measurement period in 2010 and the combined result of a all data recorded in the years 2010 and 2011. It further provides a comparison of these values with the respective theoretical calculations (Kor [12,27], Ki [11]). The frequency difference of the experimental data for the 11.15773 GHz resonance between the first year of measurements and the combined results of all recorded data may be explained by the slightly different microwave power used for the measurement period in 2010 and also by the lower statistics for this transition in the first year.

290 experimental errors have been decreased by 43% for ν_{HF}^{--} and 25% for ν_{HF}^{+} compared to
 291 previously published results [6]. The value for ν_{HF}^{+} agrees better with theory than before.
 292 Also the frequency difference $\Delta\nu_{\text{HF}}^{\pm}$ agrees with theoretical calculations. However, the
 293 experimental error for $\Delta\nu_{\text{HF}}^{\pm}$ is still very large compared to theory.

294 The measured hyperfine transition frequencies agree with theory within 0.2 – 0.5
 295 MHz (18–43 ppm). The current precision is still worse than for the most recent results
 296 with $\bar{\text{p}}^4\text{He}^+$, which gave an error of 3 ppm for the individual transition lines [5]. Due
 297 to limitations in antiproton beam quality this precision for $\bar{\text{p}}^4\text{He}^+$ is not likely to be
 298 improved anymore. However, it is also unlikely to achieve an uncertainty for $\bar{\text{p}}^3\text{He}^+$
 299 transition frequencies as small as that for $\bar{\text{p}}^4\text{He}^+$. There are eight instead of four SSHF
 300 energy levels in $\bar{\text{p}}^3\text{He}^+$ and thus the measured signal will be only about half of the signal
 301 obtained for $\bar{\text{p}}^4\text{He}^+$. Therefore much higher statistics would be required.

302 A comparison of the theoretical values for the two SSHF transitions at 11 GHz with
 303 the measurement results shows that there is a small shift in frequency towards higher
 304 values for both transitions (cf. Fig. 7). According to V. Korobov [27], this discrepancy is
 305 most likely due to the theoretical limits of the Breit-Pauli approximation that has been
 306 used for the calculations. The relative error of the theoretical frequencies is estimated
 307 to be $\alpha^2 = 5 \times 10^{-5}$. The relative error of the theoretical frequencies is estimated to
 308 be $5 \times 10^{-5} \sim 0.56$ MHz. Together with the experimental error of ~ 0.2 MHz there is

309 agreement between experiment and theory.

310 A density dependent shift could also contribute to this deviation. The density
311 dependence is found to be much smaller for an M1 transition, the electron spin-flip
312 transitions induced by the microwave, than for an E1 transition induced through laser
313 stimulation [29]. In the case of $\bar{\text{p}}^4\text{He}^+$ theoretical calculations of G. Korenman [15, 16]
314 confirmed that the density dependence is very small. Also for $\bar{\text{p}}^3\text{He}^+$ theory predicts a
315 collisional shift at the kHz level, much smaller than the experimental error bars [17].

316 For the frequency difference $\Delta\nu_{\text{HF}}^{\pm} = \nu_{\text{HF}}^{-+} - \nu_{\text{HF}}^{--}$ between the two SSHF lines around
317 11 GHz there is an agreement between both theoretical results and experiment within
318 1.5σ of the experimental error of 150 kHz (0.47%). $\Delta\nu_{\text{HF}}^{\pm}$ is important due to its
319 proportionality to the magnetic moment of the antiproton. The error of the theoretical
320 value is 1.6 kHz, which is considerably smaller than the experimental error. The reason
321 is that in theory the splitting between the transition lines can be calculated directly and
322 the errors are the same for all transitions within the hyperfine structure whereas the
323 experimental value of the splitting is received from the difference of the single transition
324 lines.

325 The two transitions at 16 GHz could not be measured anymore due to lack
326 of beamtime – even though the microwave target was readily tested and calibrated.
327 However, we came to the conclusion that the observation of these two resonance lines
328 would deliver no additional information on the investigated three-body system and
329 primarily serve to accomplish a complete measurement of the $\bar{\text{p}}^3\text{He}^+$ hyperfine structure.

330 This study with $\bar{\text{p}}^3\text{He}^+$ was considered a test of QED calculations using a more
331 complex system compared to $\bar{\text{p}}^4\text{He}^+$ and thus provide a stronger confirmation of the
332 theoretical models. With more statistics and careful investigation and accounting for
333 systematic effects such as frequency dependencies of the single parts of the microwave
334 setup the precision might realistically increase at most by a factor of two. Nonetheless,
335 this would not reach the results achieved with $\bar{\text{p}}^4\text{He}^+$ and thus not give a better
336 experimental value for the antiproton magnetic moment, i.e. a better test of CPT
337 invariance. Recently, the antiproton magnetic moment has been measured for the first
338 time using a single trapped antiproton, reaching a precision of 4.4 ppm [30] which is far
339 outside the reach of the technique presented in this work.

340 With this study the spectroscopic measurements of the hyperfine structure of $\bar{\text{p}}^3\text{He}^+$
341 are concluded. There are no further measurements planned. Based on the current
342 experimental conditions no improvement of precision can be expected. Also the theory
343 reached its limits using the calculation methods available at present.

344 Acknowledgments

345 We are grateful to Dr. V. Korobov and Dr. G. Korenman for intensive discussions on the
346 theoretical framework. Further, we want to thank our project students Matthias Fink,
347 Johannes Handsteiner, Mario Krenn, Hans-Linus Pfau und Mariana Rihl for their help
348 before and during the beamtime. This work has received funding from the Austrian

349 Science Fund (FWF): [I-198-N20] as a joint FWF-RFBR (Russian Foundation for
350 Basic Research) project, the Austrian Federal Ministry of Science and Research, the
351 Japan Society for the Promotion of Science (JSPS), the Hungarian National Science
352 Funds (OTKA K72172), the European Science Foundation (EURYI) and the Munich
353 Advanced Photonics Cluster (MAP) of the Deutsche Forschungsgemeinschaft (DFG).

354 References

- 355 [1] M. Iwasaki et al., *Phys. Rev. Lett.* **67** (1991) 1246–1249.
356 [2] T. Yamazaki et al., *Nature* **361** (1993) 238–240.
357 [3] T. Yamazaki et al., *Phys. Rep.* **366** (2002) 183–329.
358 [4] R.S. Hayano et al., *Rep. Prog. Phys.* **70(12)** (2007) 1995–2065.
359 [5] T. Pask et al., *Phys. Lett. B* **678** (2009) 55–59.
360 [6] S. Friedreich et al., *Phys. Lett. B* **700(1)** (2011) 1–6.
361 [7] M. Hori et al., *Nature* **475** (2011) 484–488.
362 [8] D. Bakalov, V.I. Korobov, *Phys. Rev. A* **57** (1998) 1662–1667.
363 [9] V.I. Korobov, D. Bakalov, *J. Phys. B* **34** (2001) 519–523.
364 [10] Yamanaka N, Kino Y, Kudo H, Kamimura M 2001 *Phys. Rev. A* **63** 012518
365 [11] Y. Kino et al., *Hyp. Int.* **146–147** (2003) 331–336.
366 [12] V. Korobov, *Phys. Rev. A* **73** (2006) 022509, *Phys. Rev. A* **73** (2006) 049902(E).
367 [13] E. Widmann et al., *Phys. Lett. B* **404** (1997) 15–19
368 [14] E. Widmann et al., *Phys. Rev. Lett.* **89** (2002) 243402.
369 [15] G.Y. Korenman, S.N. Yudin, *J. Phys. B* **39(6)** (2006) 1473–1484.
370 [16] G.Y. Korenman, S.N. Yudin, *Hyp. Int.* **194** (2009) 29–35.
371 [17] S.N. Yudin, G.Y. Korenman, *Hyp. Int.* **209** (2012) 21–24.
372 [18] S. Friedreich et al., *Hyp. Int.* **212** (2012) 167–177.
373 [19] M. Hori et al., *Nucl. Inst. Meth. A* **496** (2003) 102–122.
374 [20] M. Hori et al., *Phys. Rev. Lett.* **96** (2006) 243401.
375 [21] M. Hori et al., *Phys. Rev. Lett.* **89** (2002) 093401.
376 [22] S. Maury et al., *Nucl. Phys. B (Proc. Suppl.)* **56A** (1997) 349–357.
377 [23] O. Massiczek et al., *Nucl. Inst. Meth. A* **659** (2011) 55–60.
378 [24] S. Friedreich et al., *to be published* (2013).
379 [25] J. Sakaguchi et al., *Nucl. Inst. Meth. A* **533** (2004) 598–611.
380 [26] S. Fluegge, *Encyclopedia of physics*, Springer Verlag Berlin (1959).
381 [27] V.I. Korobov, *personal communication* (2010).
382 [28] R. Barlow, *PHYSTAT2003* (2003) arXiv:physics/0406120 [physics.data-an].
383 [29] T. Pask et al., *J. Phys. B* **41** (2008) 081008.
384 [30] J. DiSciaccia et al., *Phys. Rev. Lett.* (2013) arXiv:1301.6310 [physics.atom-ph].